

## Karhunen-Loève analysis of spatiotemporal flame patterns

Antonio Palacios,<sup>1,2,\*</sup> Gemunu H. Gunaratne,<sup>1,†</sup> Michael Gorman,<sup>1,‡</sup> and Kay A. Robbins<sup>3,§</sup>

<sup>1</sup>Department of Physics, The University of Houston, Houston, Texas 77204

<sup>2</sup>Department of Mathematics, The University of Houston, Houston, Texas 77204

<sup>3</sup>Division of Computer Science, University of Texas at San Antonio, San Antonio, Texas 78249

(Received 17 June 1997; revised manuscript received 26 January 1998)

The ability of Karhunen-Loève (KL) decomposition to identify, extract, and separate the spatial features that characterize a spatiotemporal system is demonstrated using video images from a combustion experiment and nonstationary states from a phenomenological model. Cellular flames on a circular porous plug burner exhibit a variety of stationary and nonstationary patterns. KL decomposition is used to analyze the spatiotemporal dynamics of four experimental states: one- and two-cell rotating states, two counterrotating rings, a standing-wave state, and two one-cell rotating states from numerical simulations of a phenomenological model designed to study pattern formation in a circular domain. The KL technique optimally captures the dynamics of the states by producing a linear subspace on which the reconstructed dynamics has a minimum truncation error. It identifies the dominant spatial structures whose coupling produces the observed patterns and distinguishes between uniform and nonuniform rotational motion. The implementation of this technique using video images as input is explained and the implications of symmetry in interpreting the KL analysis of the dynamics are described. [S1063-651X(98)07105-0]

PACS number(s): 82.40.Ra, 82.40.Py, 11.30.Qc, 82.20.Mj

### I. INTRODUCTION

Cellular flames form ordered patterns of concentric rings of cells when stabilized on a circular porous plug burner at low pressure. As the control parameters are varied, symmetry-breaking bifurcations are observed to dynamic states in which the cells move, exhibiting both periodic and complex dynamics. This paper demonstrates the ability of Karhunen-Loève (KL) decomposition to identify the dominant spatial structures of nonstationary flame patterns and to characterize the time dependence of the pattern of evolution. The spatial modes and their time evolution are extracted directly from two-dimensional video images produced in the experiment, in contrast to applications that use one-dimensional spatial information or that rely on time series at isolated points.

In an attempt to quantify flame dynamics using KL decomposition, a pulsating single-cell state found in methane-air flames was considered by Stone *et al.* [1]. A distinctive feature of this state is the coexistence of time-periodic pulsations with spatial chaotic motion in the orientation of the cell. To unravel the complexity, Stone *et al.* applied KL decomposition to a data set consisting of the cell boundaries. They found that the motion of the boundaries could be described by three KL eigenvectors. The reconstruction with these three eigenvectors resembled the original two-dimensional motion, and the long-term evolution indicated the presence of a limit cycle in phase space. Insight into multiple-ring formation was obtained using synthetic data to mimic the spatial structure of the cells and their motion.

In subsequent work, a boundary extraction procedure was developed and implemented to study several nonstationary states with multiple rings [2]. Four representative cases were studied: an outer rotating ring of cells concentric with an almost fixed inner ring, a single rotating ring surrounding one central cell, a ratcheting motion described by a periodic locking-unlocking mechanism of two rotating rings, and an intermittent state characterized by recurrent appearances of ordered patterns. The Karhunen-Loève analysis using boundary extraction revealed the presence of two intrinsic types of dynamics: one describing the large-scale motion of the rings and one representing the small-scale oscillatory motion of the cells. The rings appeared to be weakly coupled and the temporal evolution of the modes was used to describe the long-term evolution of the patterns.

While the analysis of cell boundaries was useful for describing the overall motion of the patterns, some important issues remain unresolved. There was little indication as to how the patterns emerge and whether the nonstationary states represent cases of uniform or nonuniform motion. Another point of interest is the study of more complicated states. Since the boundary extraction procedure is only applicable to states where the number of cells remains constant, the analysis cannot be used to describe states where cells merge and split. Many of these limitations arise because cell boundary extraction is strictly a one-dimensional technique that fails to recognize and identify the role played by the two-dimensional character of the spatial dynamics. However, the investigation of the boundary motion offers the advantage of requiring less computational time and memory than a two-dimensional analysis based directly on the images.

In a recent paper [3] we presented a phenomenological model that described general characteristics of pattern formation in a circular domain. Certain dynamical states of the experiment were reproduced in the model, and KL decomposition was used to demonstrate the similarity between the

\*Electronic address: palacios@nomad44.laptop.uh.edu

†Electronic address: gemunu@uh.edu

‡Electronic address: gorman@uh.edu

§Electronic address: krobbins@runner.utsa.edu

experimental states and the numerical results. In this paper we focus on the implementation of KL decomposition for the video image data, we relate the symmetry of the dynamical states to the symmetries of the KL eigenfunctions, and we amplify our analysis of each dynamical state by presenting phase-space trajectories of the KL coefficients.

KL decomposition optimally captures the behavior of two-dimensional flame patterns by producing a linear subspace on which the reconstructed dynamics has a minimum truncation error. Certain properties of this subspace can be used to explain the symmetries of the cells in nonstationary states [4]. The structure of the KL eigenfunctions is used to explain the formation of the patterns and to differentiate between uniform and nonuniform motion.

The experimental system is described in Sec. II. The mathematical development of KL decomposition relevant to this study is presented in Sec. III. Important aspects related to the implementation of the KL decomposition with video images are discussed and the implications of symmetry are emphasized. Representative cases of experimental flame patterns and simulations from a phenomenological model are analyzed in Sec. IV. The results are discussed in Sec. V.

## II. COMBUSTION EXPERIMENT

The experimental system consists of a circular porous plug burner that burns premixed gases inside a low pressure (0.3–0.5 atm) combustion chamber. Mixtures of isobutane and air were used for the experiments described in this paper. The pressure, flow rate, and fuel-to-oxidizer ratio are controlled to within 0.1%. A steady uniform flame appears as a circular luminous disk, 5.62 cm in diameter and 0.5 mm thick. The flame front forms roughly 5 mm above the surface of the burner.

A Dage-MTI charge coupled device camera, mounted vertically on top of the combustion chamber, is used to record the evolution of the flame front. A distinctive feature of premixed flames, as a system exhibiting spatiotemporal dynamics, is that an important dynamical variable is the local temperature which can be measured using the emitted chemiluminescence from the flame front. The spatial and temporal resolution, the time interval, and the dynamic range are limited only by the recording device. Images of  $640 \times 480$  pixel resolution, taken at 1/30-sec intervals with a 7-bit dynamic range, are typical for dynamics recorded on S-VHS video tape.

Upon changes of parameters (type of fuel, pressure, total flow, and equivalence ratio) the flame front forms ordered patterns of concentric rings of cells. Brighter cells correspond to hotter regions on the burner. They are separated by darker regions corresponding to cusps and folds that extend an additional 5 mm away from the surface of the burner. As the parameters are varied, the  $O(2)$  symmetric uniform state bifurcates to other stationary states or to dynamical states with less spatiotemporal symmetry [5]. In the former case, new ring structures emerge with different spatial symmetries and various numbers of cells. In this paper we consider four nonstationary states: a single rotating cell, two rotating cells, two counterrotating rings, and a standing wave of two cells. Figure 1 shows four sequential frames of videotape from these states. Each state was reached by an abrupt change in

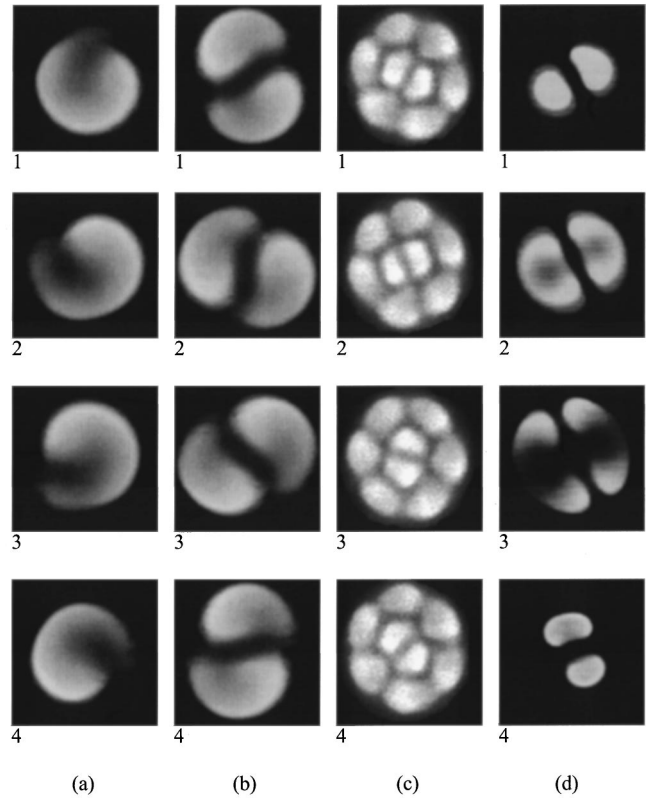


FIG. 1. Four sequential frames of videotape of four different experimental cellular flame states: (a) a single rotating cell, (b) two rotating cells, (c) counterrotating rings, and (d) a standing wave between two cells.

the control parameters during a coarse survey of parameter space.

## III. KARHUNEN-LOÈVE DECOMPOSITION

Karhunen-Loève decomposition is a well-known technique for determining an optimal basis for a data set [6–10]. This section reviews the definitions and properties of KL decomposition relevant to this paper and discusses how the method can be applied to image data in order to separate spatial and temporal behavior.

Consider a sequence of observations represented by the scalar functions  $u(\mathbf{x}, t_i), i = 1, \dots, M$ . The functions  $u$  are assumed to be  $L^2$  on a domain  $D$  that is a bounded subset of  $R^n$ . The functions are parametrized by  $t_i$ , which represents time in this application. The (time) average of the sequence, defined as  $\bar{u}(\mathbf{x}) = \langle u(\mathbf{x}, t_i) \rangle = (1/M) \sum_{i=1}^M u(\mathbf{x}, t_i)$ , is assumed to be zero. The KL decomposition extracts time-independent orthonormal basis functions  $\Phi_k(\mathbf{x})$  and time-dependent orthonormal amplitude coefficients  $a_k(t_i)$  such that the reconstruction

$$u(\mathbf{x}, t_i) = \sum a_k(t_i) \Phi_k(\mathbf{x}), \quad i = 1, \dots, M, \quad (3.1)$$

is optimal in the sense that the average least-squares truncation error

$$\varepsilon_N = \left\langle \left\| u(\mathbf{x}, t_i) - \sum_{k=1}^N a_k(t_i) \Phi_k(\mathbf{x}) \right\|^2 \right\rangle \quad (3.2)$$

is always a minimum for any given number  $N$  of basis functions over all possible sets of orthogonal functions.

The functions  $\Phi_k(\mathbf{x})$ , called *empirical eigenfunctions*, *coherent structures*, or *KL modes*, are the eigenvectors of the *two-point spatial correlation function*

$$r(\mathbf{x}, \mathbf{y}) = \frac{1}{M} \sum_{i=1}^M u(\mathbf{x}, t_i) u^T(\mathbf{y}, t_i). \quad (3.3)$$

### A. Application to image data

KL decomposition can be generally applied to find an optimal basis for a data set. To separate the spatial and the time behavior for a physical system, each point in the data set should represent an observation of the spatial state of the system at a particular time. KL decomposition is applied to the observations to find an optimal basis for the spatial observations. The data set is projected on the resulting KL basis functions to obtain the time behavior in much the same way as normal mode expansions are used for partial differential equations. The KL technique is based purely on the observations and thus has the advantage of not requiring knowledge of an underlying model equation or normal modes.

In practice the state of a numerical model is only available at discrete spatial grid points and so the observations that form the data set are vectors rather than continuous functions. In other words,  $D = (x_1, x_2, \dots, x_N)$ , where  $x_j$  is the  $j$ th grid point and  $u(\mathbf{x}, t_i)$  is the vector  $\mathbf{u}_i = (u(x_1, t_i), u(x_2, t_i), \dots, u(x_N, t_i))^T$ .

Experimental data also undergoes a discretization process when it is acquired for processing. In the case of the combustion experiment, images of the flame front were digitized to obtain the observations at different times. Each image is a  $w \times h = N$  array of pixels. A pixel is a scalar value in the interval  $[0, 255]$ . An image can be converted to a vector by ordering the pixel values in row major form [e.g., the pixel  $(j, k)$  in the image is stored in the position  $n = j \times w + k$  in the vector].

### B. Method of snapshots

A popular technique for finding the eigenvectors of Eq. (3.3) is the *method of snapshots* developed by Sirovich [10]. It was introduced as an efficient method when the resolution of the spatial domain ( $N$ ) is higher than the number of observations ( $M$ ). The method of snapshots is based on the fact that the data vectors  $\mathbf{u}_i$  and the eigenvectors  $\Phi_k$  span the same linear space (see [6,10] for details). This implies that the eigenvectors can be written as a linear combination of the data vectors

$$\Phi_k = \sum_{i=1}^M v_i^k \mathbf{u}_i. \quad (3.4)$$

After substitution in the eigenvalue problem  $r(\mathbf{x}, \mathbf{y})\Phi(\mathbf{y}) = \lambda \Phi(\mathbf{x})$ , the coefficients  $v_i^k$  are obtained from the solution of

$$C\mathbf{v} = \lambda \mathbf{v}, \quad (3.5)$$

where  $\mathbf{v}^k = (v_1^k, \dots, v_M^k)$  is the  $k$ th eigenvector of Eq. (3.5) and  $C$  is a symmetric  $M \times M$  matrix defined by  $[c_{ij}] = (1/M)(\mathbf{u}_i, \mathbf{u}_j)$ , where  $(\cdot, \cdot)$  denotes the standard vector inner product  $(\mathbf{u}_i, \mathbf{u}_j) = u(x_1, t_i)u(x_1, t_j) + \dots + u(x_N, t_i)u(x_N, t_j)$ . In this way an  $N \times N$  eigenvalue problem [the eigenvectors of Eq. (3.3)] is reduced to computing the eigenvectors of an  $M \times M$  matrix, a preferable task if  $N \gg M$ . Throughout the remaining of this work,  $M$  will denote the number of measurements of a laboratory or numerical experiment and  $N$  will represent the maximum number of KL eigenfunctions employed in a particular reconstruction of an experiment. The results presented in Sec. IV were obtained with an implementation of the method of snapshots.

### C. Properties of KL decomposition

Since the kernel is Hermitian  $r(\mathbf{x}, \mathbf{y}) = r^*(\mathbf{y}, \mathbf{x})$ , it admits, according to the Riesz theorem [11], a diagonal decomposition of the form

$$r(\mathbf{x}, \mathbf{y}) = \sum_{k=1}^N \lambda_k \Phi_k(\mathbf{x}) \Phi_k^*(\mathbf{y}). \quad (3.6)$$

This fact is particularly useful when finding the KL modes analytically. They can be read off from the diagonal decomposition (3.6).

The temporal coefficients  $a_k(t_i)$  are calculated by projecting the data set on each of the eigenfunctions

$$a_k(t_i) = (u(\mathbf{x}, t_i), \Phi_k(\mathbf{x})), \quad i = 1, \dots, M. \quad (3.7)$$

It can be shown that both temporal coefficients and eigenfunctions are uncorrelated in time and space, respectively [6,10].

*Proposition 1.* The KL modes  $\{\Phi_k(\mathbf{x})\}$  with corresponding temporal coefficients  $\{a_k(t_i)\}$  satisfy the following orthogonality properties: (i)  $\Phi_j^*(\mathbf{x})\Phi_k(\mathbf{x}) = \delta_{jk}$  and (ii)  $\langle a_j(t_i) a_k^*(t_i) \rangle = \delta_{jk} \lambda_j$ , where  $\delta_{jk}$  represents the Kronecker delta function.

Property (ii) is obtained when the terms in the diagonal decomposition (3.6) are compared with the expression  $r(\mathbf{x}, \mathbf{y}) = \sum \langle a_j(t_i) a_k^*(t_i) \rangle \Phi_j(\mathbf{x}) \Phi_k^*(\mathbf{y})$ . The non-negative and self-adjoint properties of  $r(\mathbf{x}, \mathbf{y})$  imply that all eigenvalues are non-negative and can be ordered accordingly:  $\lambda_1 \geq \lambda_2 \geq \dots \geq 0$ . Statistically speaking,  $\lambda_k$  represents the variance of the data set in the direction of the corresponding KL mode,  $\Phi_k(\mathbf{x})$ . In physical terms, if  $u$  represents a component of a velocity field, then  $\lambda_k$  measures the amount of kinetic energy captured by the respective KL mode  $\Phi_k(\mathbf{x})$ . In this sense, the energy measures the contribution of each mode to the overall dynamics.

*Definition 1.* The total energy captured in a Karhunen-Loève decomposition of a numerical or experimental data set is defined as the sum of all eigenvalues

$$E = \sum_{k=1}^N \lambda_k. \quad (3.8)$$

The relative energy captured by the  $k$ th mode,  $E_k$  is defined by

$$E_k = \frac{\lambda_k}{\sum_{j=1}^N \lambda_j}. \quad (3.9)$$

The cumulative sum of relative energies  $\sum E_k$  approaches one as the number of modes in the reconstruction increases.

Spatiotemporal systems are capable of producing different kinds of behavior including periodic, quasiperiodic, and non-periodic motion in space and time. In some cases, the KL decompositions of qualitatively different states may produce seemingly similar spectra. However, the decomposition can still be used to differentiate between different solutions. One possibility is to apply the KL decomposition to the state of interest and then use the KL energy spectrum to calculate the entropy of the data set. The entropy is a measure of order or disorder and provides an objective way of classifying the complexity in experimental or numerical data.

*Definition 2.* The entropy  $\mathcal{E}$  of a KL decomposed data set  $u$  can be calculated from its energy spectrum according to

$$\mathcal{E}(u) = - \lim_{N \rightarrow \infty} \frac{1}{\ln N} \sum_{k=1}^N E_k \ln E_k, \quad (3.10)$$

where  $\ln N$  is a normalization factor that allows comparisons between different data sets.

The entropy, as defined by Eq. (3.10), measures the energy distribution among the modes in the KL spectra and varies between 0 and 1, as the number of modes increases. The entropy is low when the energy is concentrated in a few modes. A zero entropy indicates that only one eigenfunction, with maximal energy  $E_1 = 1$ , is needed to reproduce the dynamics. The entropy approaches 1 when the energy spreads across a large number of modes, indicating complex behavior.

Equation (3.2) states that Karhunen-Loève decomposition produces a basis that minimizes the least-squares truncation error. This property can also be stated in terms of the energy captured by the KL modes.

*Proposition 2.* Let  $\{a_k(t_i), \Phi_k(\mathbf{x})\}$  be the KL basis pairs obtained from a scalar field  $u(\mathbf{x}, t_i)$  satisfying Eqs. (3.1), (3.6), and (3.7). Let  $\{b_k(t_i), \Psi_k(\mathbf{x})\}$  be any arbitrary orthonormal basis pair satisfying Eq. (3.1). The KL basis is optimal in the sense that the total cumulative energy captured by the sequence  $\{a_k(t_i), \Phi_k(\mathbf{x})\}$  is always greater than or equal to the total cumulative energy captured by  $\{b_k(t_i), \Psi_k(\mathbf{x})\}$  provided the number of eigenfunctions (respecting their ordering from most to least energetic) employed is the same. Formally

$$\sum_{k=1}^N E_k = \sum_{k=1}^N \langle a_k(t_i) a_k^*(t_i) \rangle = \sum_{k=1}^N \lambda_k \geq \sum_{k=1}^N \langle b_k(t_i) b_k^*(t_i) \rangle. \quad (3.11)$$

#### D. Consequences of symmetry

One motivation for applying KL decomposition is to obtain information about the long-term behavior of the system. Suppose that this behavior is captured by an attractor, denoted by  $\mathcal{A}$  (see [12] for a precise definition). Assume also that scalar measurements of the system  $g(\mathbf{x}, t_i)$ ,  $i$

$= 1, \dots, M$ , are provided. In practice, one must first compute the average  $\bar{g}(\mathbf{x}) = (1/M) \sum_{i=1}^M g(\mathbf{x}, t_i)$  in order to produce a new set of measurements  $u(\mathbf{x}, t_i) = g(\mathbf{x}, t_i) - \bar{g}(\mathbf{x})$  with zero average. Let  $\Gamma$  denote the group of symmetries of the system of interest. The symmetries of the attractor form a subgroup of  $\Gamma$  defined by

$$\Gamma_{(\mathcal{A})} = \{\gamma \in \Gamma \mid \gamma \mathcal{A} = \mathcal{A}\}. \quad (3.12)$$

The critical observation is that the symmetries of the attractor  $\mathcal{A}$  appear as symmetries of the time average  $\bar{g}(\mathbf{x})$  independently of the symmetries of the instantaneous scalar field  $g(\mathbf{x}, t_i)$  [14]. Unfortunately, the converse is not always true. The symmetries of the time average do not necessarily reflect the symmetries of the underlying attractor. Furthermore, the KL decomposition satisfies the following symmetry properties.

*Proposition 3.* Let  $\{\Phi(\mathbf{x})\}$  be the KL eigenfunctions satisfying the eigenvalue problem  $\langle u(\mathbf{x}, t) u^*(\mathbf{y}, t) \rangle \Phi(\mathbf{y}) = \lambda \Phi(\mathbf{x})$ . Then (i)  $\langle \gamma u(\mathbf{x}, t) \gamma u^*(\mathbf{y}, t) \rangle \gamma \Phi(\mathbf{y}) = \lambda [\gamma \Phi(\mathbf{x})]$  for all  $\gamma \in \Gamma$ , (ii)  $\langle \sigma u(\mathbf{x}, t) \sigma u^*(\mathbf{y}, t) \rangle = \langle u(\mathbf{x}, t) u^*(\mathbf{y}, t) \rangle$  for all  $\sigma \in \Gamma_{(\mathcal{A})}$ , and (iii)  $\langle u(\mathbf{x}, t) u^*(\mathbf{y}, t) \rangle \sigma \Phi(\mathbf{y}) = \lambda [\sigma \Phi(\mathbf{x})]$  for all  $\sigma \in \Gamma_{(\mathcal{A})}$ .

Property (i) establishes that the eigenfunctions in the KL decomposition of  $\gamma u(\mathbf{x}, t)$  are those of  $u(\mathbf{x}, t)$  under the action of  $\gamma$ . This property explains the observation that the KL decomposition of a periodic data set is not unique. If  $\Phi(\mathbf{x})$  is an eigenfunction, so is  $\gamma \Phi(\mathbf{x})$  for all  $\gamma \in \Gamma$ . Which one is then chosen? In the case of experimental or computational data, the answer depends on how the data are collected. Performing the decomposition with different initial conditions may produce a rotated version of  $\Phi(\mathbf{x})$ . Nevertheless, the important point is to realize that they are all symmetrically related. Properties (ii) and (iii) indicate that the KL kernel and its eigenvectors have at least the same symmetries as the attractor.

#### E. Traveling waves and KL decomposition

Consider a periodic traveling wave represented by a periodic function in the form  $u(\mathbf{x}, t) = f(x - ct)$ , where  $c$  denotes the speed of the wave. As noted in [13], the KL decomposition coincides with the Fourier decomposition

$$f(x - ct) = \sum_{k=-\infty}^{\infty} c_k e^{-ik\pi(x-ct)}. \quad (3.13)$$

The alternative form

$$f(x - ct) = \sum_{k=0}^{\infty} \sqrt{a_k^2 + b_k^2} [\cos(k\pi ct + \alpha_k) \sin(k\pi x) - \sin(k\pi ct + \alpha_k) \cos(k\pi x)] \quad (3.14)$$

shows the KL modes explicitly. Here  $c_k = (a_k + b_k i)/2$  are the Fourier coefficients of  $f(x - ct)$  with phase  $\alpha_k = \tan^{-1}(-a_k/b_k)$ . The KL modes can be written as ordered pairs of the form  $\{\Phi_{2k-1}, \Phi_{2k}\} = \{\cos(k\pi x), \sin(k\pi x)\}$ . The traveling wave is produced by the coupling of pairs of modes that contain the same energy and maintain a constant relative phase.

By analogy with pure periodic traveling waves, adjacent KL modes with the same symmetry and equivalent energy may be associated with traveling-wave solutions. Such adjacent modes are called *coupling modes*.

*Definition 3.* Let  $u(\mathbf{x}, t_i) = \sum_{k=1}^N a_k(t_i) \Phi_k(\mathbf{x})$ ,  $i = 1, \dots, M$ , represent the KL decomposition of a data set. The relative phase of KL eigenfunctions  $m$  and  $n$ ,  $m \neq n$ , is defined by

$$\phi_{mn}(t_i) = \tan^{-1} \left( -\frac{a_n(t_i)}{a_m(t_i)} \right). \quad (3.15)$$

The *relative phase*  $\phi_{mn}$  between KL modes  $\Phi_m$  and  $\Phi_n$  has the following geometric interpretation. If the temporal coefficients  $a_m(t_i)$  and  $a_n(t_i)$  are represented by a point in a phase plane plot, then  $\phi_{mn}(t_i)$  are observations of the angular displacement of the plotted point as it moves in the phase plane. A relative phase between coupling modes that is linear indicates an underlying traveling-wave solution that is moving uniformly. Similarly, a nonlinear relative phase indicates a modulated traveling wave or perhaps more complicated behavior.

In the traveling wave described by Eq. (3.14), we find that  $\phi_{(2k-1)(2k)}(t) = k\pi ct + \alpha_k \pmod{\pi}$  is the relative phase between coupling modes. Observe that this relative phase  $\phi_{(2k-1)(2k)}$  is not uniquely defined. An alternative expression

$$f(x - ct) = \sum_{k=0}^{\infty} \sqrt{a_k^2 + b_k^2} [\cos(k\pi ct) \sin(k\pi x + \alpha_k) - \sin(k\pi ct) \cos(k\pi x + \alpha_k)] \quad (3.16)$$

shows that  $\phi_{(2k-1)(2k)}(t) = k\pi ct \pmod{\pi}$  is also possible. From the viewpoint of symmetry, each pair of KL modes  $\{\cos(k\pi x), \sin(k\pi x)\}$  forms an irreducible subspace for the representation of the traveling wave. Any left-right shift of these modes, with temporal coefficients shifted accordingly, can also be used as a KL basis.

## IV. RESULTS

### A. Computational details

For each of the flame patterns analyzed in this section, a representative sequence of video images was digitized. Depending on the speed of the motion, a capturing rate of 15 or 30 frames per second was employed. Sufficient frames ( $\sim 200$ ) for each state were captured to obtain a well-defined time-average pattern and several full multiples of the period. Each image frame was then scaled to  $64 \times 64$  pixels and converted from an audio-video interlace movie format to a stream of intensity values ranging from 0 to 255. The KLTOOL software package [15] was used to perform an interactive KL decomposition. For each case analyzed, a computer animation comparing reconstructions from different KL modes can be found on the World Wide Web [16].

### B. Single-ring rotating states

Ordered states of concentric rings of cells bifurcate to states in which entire rings of cells rotate either clockwise or counterclockwise [5]. Rotating states, which are typically found in isobutane-air flames, represent traveling-wave solu-

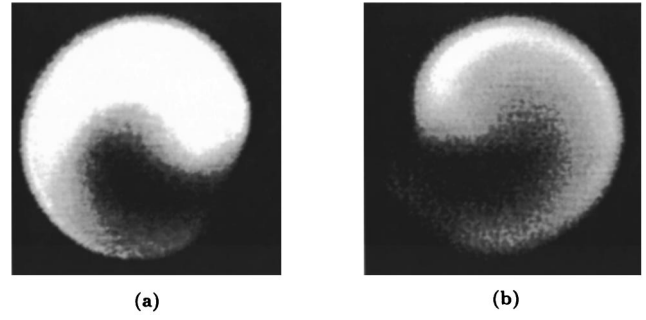


FIG. 2. Examples of one-cell states from the experiment rotating (a) clockwise and (b) counterclockwise.

tions of the underlying system. It has been demonstrated [17,18] that in one-dimensional interfaces, traveling cells appear as a result of a parity breaking in which the cells lose their left-right symmetry. A manifestation of parity breaking in a two-dimensional system is demonstrated by these rotating cellular flame states [19]. Figure 2(a) shows an experimental state in which a single cell executes clockwise rotation, while Fig. 2(b) shows a related state in which a single cell rotates in the counterclockwise direction.

### 1. One-cell rotating state: Experiment

The single rotating cell state shown in Fig. 2(a) was chosen for the KL analysis. Sixty frames, digitized at a rate of 30 frames/sec, contain about seven complete revolutions of the cell. Figure 3(a) shows some instantaneous snapshots, Fig. 3(b) shows the eigenfunctions extracted by the KL decomposition, and Fig. 3(c) shows the KL reconstructions based on the corresponding eigenfunctions. The top snapshot in

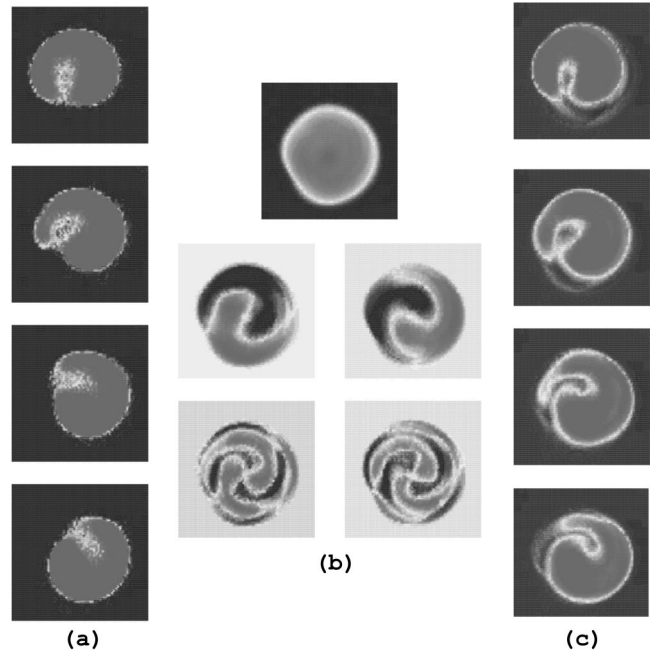


FIG. 3. A KL decomposition of a rotating one-cell state from the experiment: (a) four instantaneous snapshots showing a clockwise rotating cell; (b) the time average of the data set appears at the top, followed (from left-to-right and top-to-bottom) by the four most energetic modes  $\Phi_1$ ,  $\Phi_2$ ,  $\Phi_3$ , and  $\Phi_4$ ; and (c) the reconstruction of the dynamics using the four most energetic KL modes.

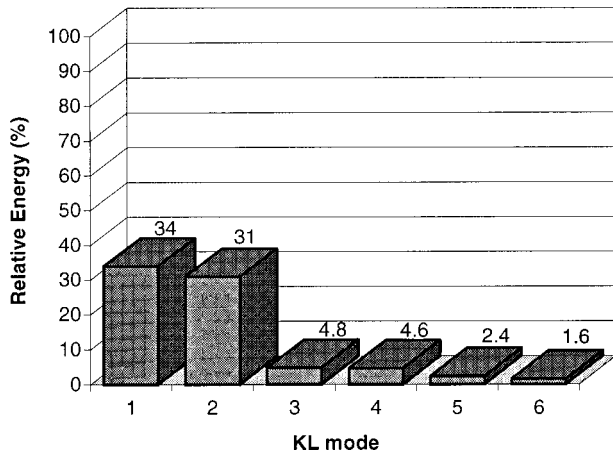


FIG. 4. Energy spectrum for the KL decomposition of the rotating one-cell state of Fig. 3(a).

Fig. 3(b) is the time average of the images. The four most energetic KL modes  $\Phi_1$ ,  $\Phi_2$ ,  $\Phi_3$ , and  $\Phi_4$  are depicted below the time average (from left to right and top to bottom, respectively) in Fig. 3(b). The KL reconstruction using the first two modes  $\Phi_1$  and  $\Phi_2$  captures the rotation of the cell. The reconstruction with the first four KL modes [Fig. 3(c)] further improves the representation of the motion and shape of the cell. The similarity to the original state is clearly visible.

The KL energy spectra (Fig. 4) shows that 75% of the total energy is captured by the first four modes. The energy is almost equally distributed between  $\Phi_1$  and  $\Phi_2$ , indicating that they form a coupling pair. Similarly,  $\Phi_3$  and  $\Phi_4$  also form a coupling pair. The remaining modes capture less energy (25%) and contain high-dimensional information. A 75% cutoff between low-dimensional and high-dimensional dynamics has also been observed in the KL analysis of other experiments [20].

The long-term motion of a cell can be understood from the temporal coefficients  $a_1(t)$ ,  $a_2(t)$ ,  $a_3(t)$ , and  $a_4(t)$  associated with the most energetic KL modes (Fig. 5). The sinusoidal nature of these projections is evidenced by their time plots [Figs. 5(a) and 5(b)]. The  $\{a_1(t), a_2(t)\}$  pair forms a traveling wave, which results in a uniform rotation of 3.3 rev/sec. The  $\{a_3(t), a_4(t)\}$  pair oscillates at twice the frequency of the first pair [compare Fig. 5(a) with Fig. 5(b)], indicating their role as a higher spatial harmonic in defining the cell shape. This phenomenon can be understood from the spatial symmetries of the two pairs of modes.  $\Phi_1$  and  $\Phi_2$  have (approximately)  $D_1$  symmetry, meaning that they will return to their original pattern in one complete rotation. In contrast,  $\Phi_3$  and  $\Phi_4$  have  $D_2$  symmetry. They return to their original pattern in half a revolution. In general, the primary spatial harmonic of a periodic pattern with  $D_n$  symmetry will have  $D_{2n}$  symmetry. The harmonic only has to rotate half as far as the original mode to reestablish the original pattern.

Figure 6(a) shows the behavior of  $\phi_{12}$ , the relative phase between the first pair of KL modes. The nearly linear behavior of the relative phase indicates that the cell is rotating uniformly.

The  $SO(2)$  or  $O(2)$  symmetry of the time average in Fig. 3(b) [on the plane  $SO(2)$  and  $O(2)$  symmetries cannot be distinguished] reflects the symmetry of the burner, even though none of the instantaneous snapshots of Fig. 3(a) has

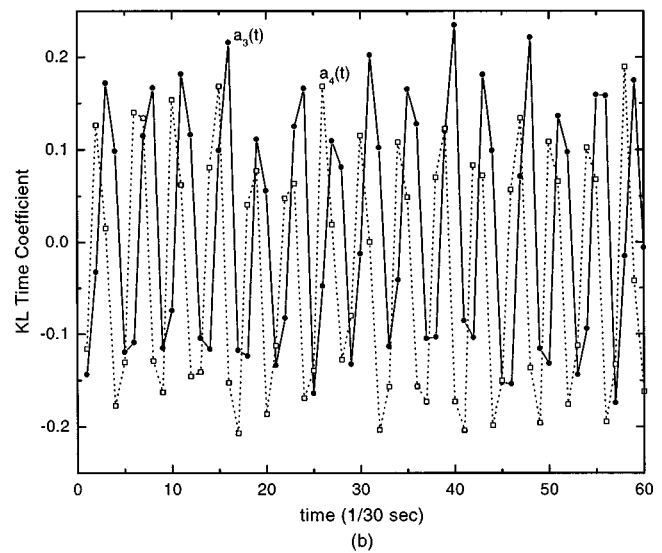
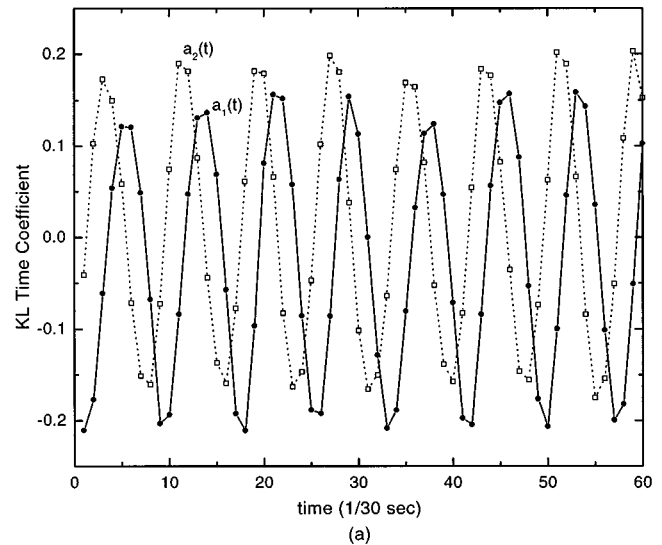


FIG. 5. Temporal coefficients for the four most energetic modes in the KL decomposition of a single rotating cell shown in Fig. 3: (a) time plots of  $a_1(t)$  and  $a_2(t)$  and (b) time plots of  $a_3(t)$  and  $a_4(t)$ .

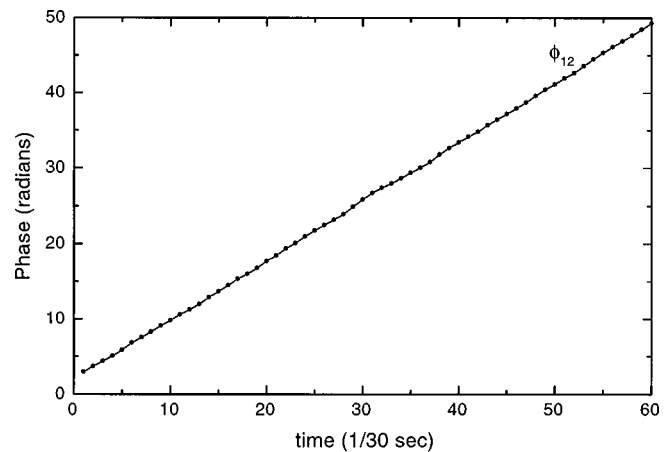


FIG. 6. Behavior of the relative phase  $\phi_{12}(t)$  for the one-cell rotating state from the experiment.

this symmetry. Each of the pairs of KL modes  $\{\Phi_1, \Phi_2\}$  and  $\{\Phi_3, \Phi_4\}$  forms an irreducible subspace [4] under the action of the symmetries of the system,  $\Gamma = O(2) \times S^1$  for the circular burner.  $S^1$  is the circle group that accounts for the temporal phase-shift symmetries of periodic states. The invariance of these subspaces implies that if a cellular state has certain symmetries at one instant of time, then it must have the same symmetries at all times. Consequently, any cellular state with a reflectional symmetry must have the same symmetry at all times and it therefore cannot rotate.

Also note that based on Proposition 3(i), these irreducible subspaces are not unique. The particular subspace representing each symmetry is selected by initial conditions. Once a particular subspace is chosen, the KL reconstructed dynamics on that subspace corresponds to a unique branch of periodic solutions with group symmetry  $\Sigma \subset \Gamma$ . According to the equivariant Hopf theorem with  $O(2) \times S^1$  symmetry [4], two types of periodic states can appear with  $\Sigma$  symmetry: rotating waves and standing waves. The one-cell rotating state and the other states in this section are examples of rotating waves.

## 2. One-cell rotating state: Phenomenological model

Numerical simulations of a phenomenological model [3] that is closely related to flame dynamics have demonstrated the formation of both stationary and nonstationary states. These states emerge as a result of symmetry-breaking bifurcations in which several spatial modes couple and compete for existence. The model describes the evolution of two coupled, diffusive spatiotemporal fields  $u(\mathbf{x}, t)$  and  $v(\mathbf{x}, t)$  through

$$\begin{aligned} u_t &= \kappa_1 \nabla^2 u + (B-1)u + A^2 v - \eta u^3 - \nu_1 (\nabla u)^2, \\ v_t &= \kappa_2 \nabla^2 v - Bu - A^2 v - \eta v^3 - \nu_2 (\nabla v)^2, \end{aligned} \quad (4.1)$$

where  $\kappa_1$  and  $\kappa_2$  are the diffusion coefficients of the two linearly coupled fields. The cubic terms control the growth of the linearly unstable modes. The nonlinear gradient terms render the model nonvariational and are similar to the nonlinear term of the Kuramoto-Sivashinsky equation [21,22], which is often used to model flame dynamics. In order to simulate the circular geometry of the experimental burner, the integration of Eqs. (4.1) is carried out in polar coordinates over a circular grid of radius  $R$ . Small changes in the radius  $R$  can produce qualitatively different flame patterns. This observation leads us to consider the radius as a distinguished bifurcation parameter.

Figure 7(a) shows four snapshots of a single-cell state simulated with Eqs. (4.1) for parameter values ( $\eta=2.0$ ,  $\nu_1=0.5$ ,  $\nu_2=1.0$ ,  $\kappa_1=0.2$ ,  $\kappa_2=2.0$ ,  $A=5.0$ ,  $B=6.8$ , and  $R=1.35$ ). It consists of a single cell rotating clockwise that does not change its shape. The KL decomposition of a complete period produces an  $O(2)$  invariant time-average pattern [Fig. 7(b)] and four KL modes  $\Phi_1$ ,  $\Phi_2$ ,  $\Phi_3$ , and  $\Phi_4$  (depicted from left to right and top to bottom, respectively). A similar KL spectrum indicates that the first two modes  $\Phi_1$  and  $\Phi_2$  capture about 94% of the energy as compared to 65% (considering only the first two modes) for the experimental one-cell rotating state shown in Fig. 3(a). Only two modes are necessary to reconstruct the dynamics and the

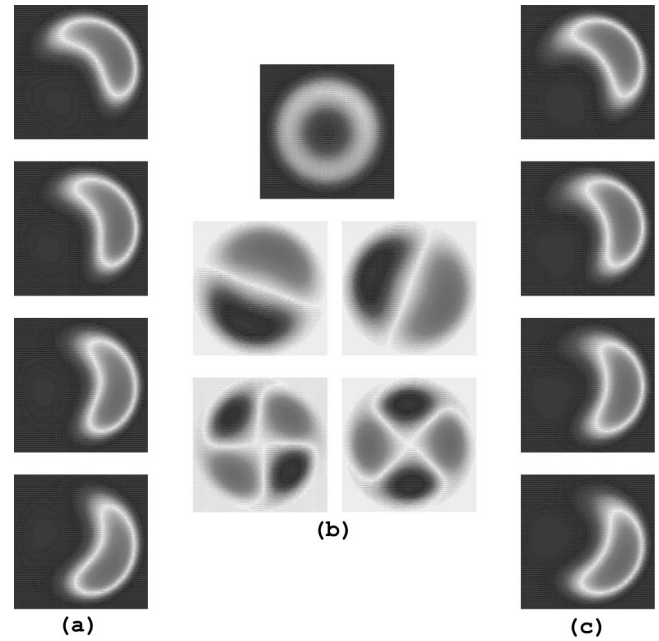


FIG. 7. (a) Four snapshots of a uniformly rotating one-cell state produced from simulations of Eqs. (4.1), (b) the time average and (from left-to-right and top-to-bottom) the four most energetic KL modes, and (c) reconstruction of the dynamics using the four most energetic KL modes.

remaining modes affect other aspects such as cell shape. Nearly 100% of the energy is captured by the first four modes. The reconstruction with these four KL modes is shown in Fig. 7(c).

The details of the temporal behavior of the cell are extracted from the KL projections. Figure 8(a) shows phase plots of  $a_1(t)$  vs  $a_2(t)$ ,  $a_3(t)$  vs  $a_4(t)$ , and  $a_1(t)$  vs  $a_3(t)$ . The first pair indicates the uniform rotation of the cell. The second pair indicates a periodic oscillation at twice the frequency of the dominant pair. The plots of the relative phases for each pair of KL modes shown in Fig. 8(b) confirm this relationship.

The group-theoretical interpretation of this mode is similar to that of the one-cell experimental state. The time average has  $O(2)$  symmetry.  $\Phi_1$  and  $\Phi_2$ , which have  $D_1$  symmetry, form an irreducible space under the action of  $\Gamma$ . Similarly,  $\Phi_3$  and  $\Phi_4$  have  $D_2$  symmetry and form an irreducible space under the action of  $\Gamma$ .

## 3. Modulated rotation: Phenomenological model

Figure 9(a) shows a solution of Eqs. (4.1) when  $R=1.37$  rather than 1.35. The solution contains a single cell that changes its shape periodically while rotating clockwise. The symmetries of the time average and the dominant KL modes have not changed significantly from the uniformly rotating case. The four most energetic modes  $\Phi_1$ ,  $\Phi_2$ ,  $\Phi_3$ , and  $\Phi_4$  capture 98% of the total energy in the associated KL spectrum. The second pair  $\{\Phi_3, \Phi_4\}$  contains more energy than the corresponding pair for the uniformly rotating case, but the general characteristics of the spectrum are similar. Figure 10(a) shows phase plane plots of the temporal coefficients  $a_1(t)$  vs  $a_2(t)$ ,  $a_3(t)$  vs  $a_4(t)$ , and  $a_1(t)$  vs  $a_3(t)$ . The phase portraits of this modulated rotation are considerably

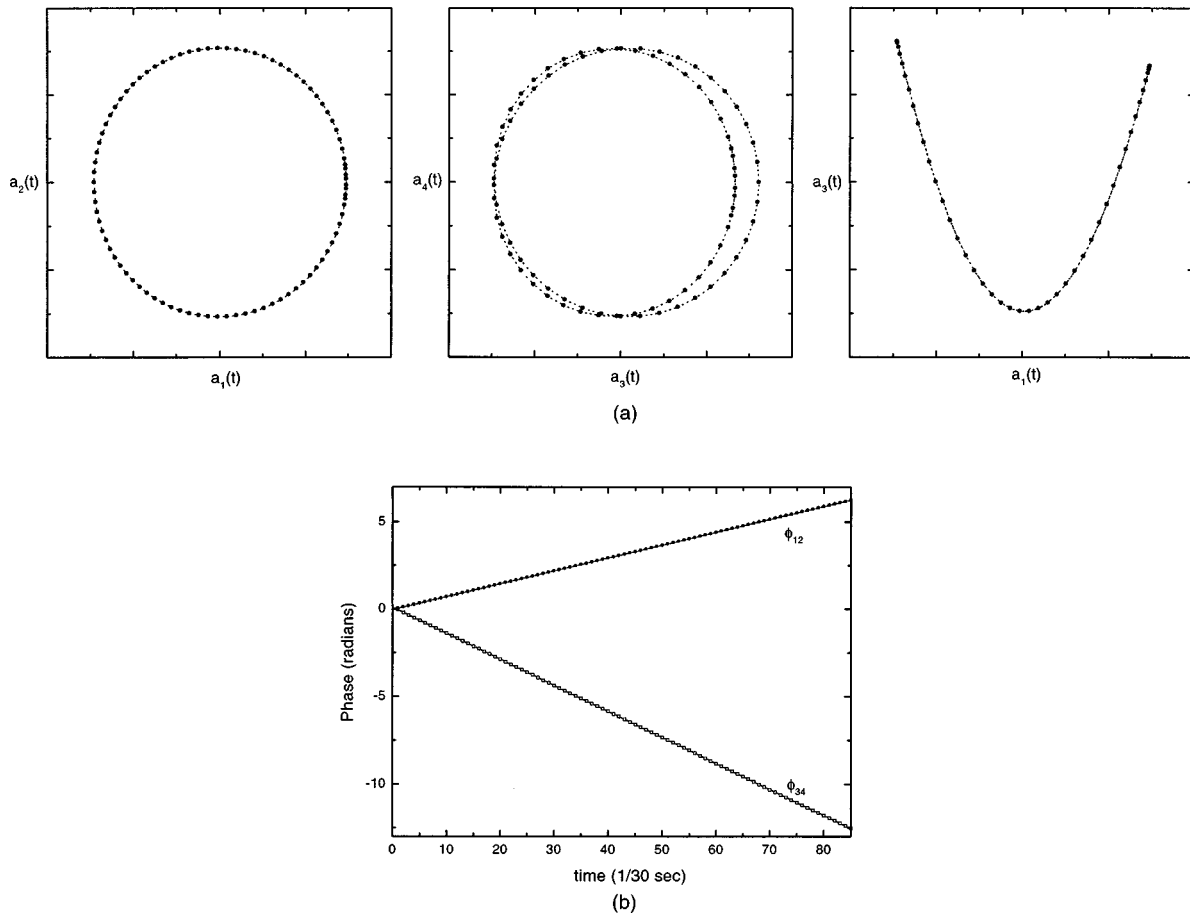


FIG. 8. Evolution of the temporal coefficients of the uniformly rotating one-cell state of Fig. 7(a): (a) from left to right phase plane plots of  $a_1(t)$  vs  $a_2(t)$ ,  $a_3(t)$  vs  $a_4(t)$ , and  $a_1(t)$  vs  $a_3(t)$  and (b) a time plot of  $\phi_{12}(t)$  and  $\phi_{34}(t)$ .

more intricate than those corresponding to the uniform rotation shown in Fig. 8(a). Figure 10(b) shows the plot of the relative phase of the two most energetic KL modes. The modulations in the angular speed of the cell are clearly visible.

#### 4. Two-cell rotating state: Experiment

Another state observed in the combustion experiment consists of two rotating cells. Figure 11(a) shows four instantaneous snapshots of two cells rotating counterclockwise. The reflectional asymmetry of the cells is again visible. Figure 11(b) shows an  $O(2)$  symmetric time average followed (from left to right and top to bottom) by the four most energetic KL modes  $\Phi_1$ ,  $\Phi_2$ ,  $\Phi_3$ , and  $\Phi_4$ . The energy distribution in the associated KL spectrum is almost identical to the spectrum in the experimental one-cell state analyzed above, with 83% of the total energy being captured by the first four modes. Notice that the time average of the two-cell rotating state is still  $O(2)$ . The symmetry of the lowest KL modes is now  $D_2$  in contrast to the one-cell rotating case where it was  $D_1$ . In general, we observe that modes with  $n$  cells have lowest KL modes with at least  $D_n$  symmetry.

The phase plane plots of  $a_1(t)$  vs  $a_2(t)$ ,  $a_3(t)$  vs  $a_4(t)$ , and  $a_1(t)$  vs  $a_3(t)$  indicate approximately uniform rotation with the second pair at twice the frequency. This observation is confirmed by a plot of the relative phase of the first pair shown in Fig. 12(b).

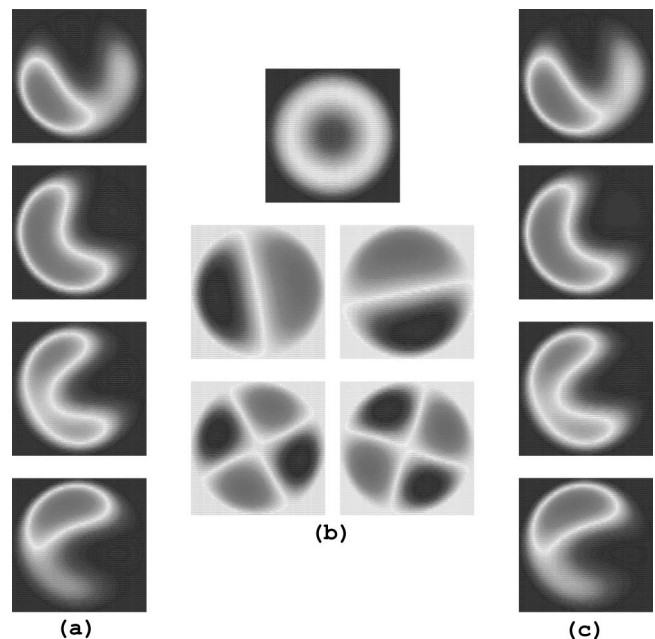


FIG. 9. (a) Four snapshots of a nonuniformly rotating one-cell state produced from simulations of Eqs. (4.1), (b) the time-average pattern and (from left-to-right and top-to-bottom) the four most energetic KL modes, and (c) reconstruction of the dynamics using the four most energetic KL modes.



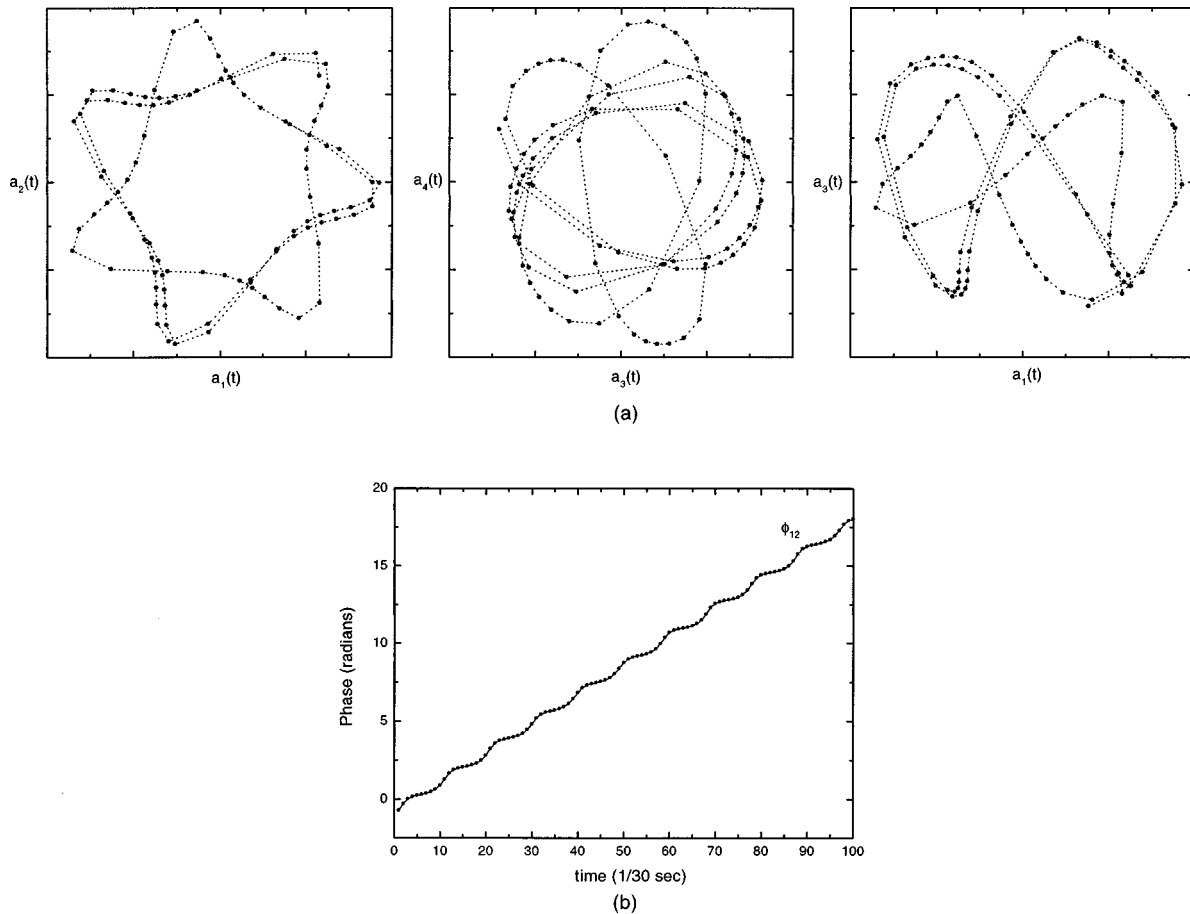


FIG. 10. Evolution of the temporal coefficients of the nonuniformly rotating one-cell state of Fig. 9(a): (a) from left to right phase plane plots of  $a_1(t)$  vs  $a_2(t)$ ,  $a_3(t)$  vs  $a_4(t)$ , and  $a_1(t)$  vs  $a_3(t)$  and (b) a time plot of  $\phi_{12}(t)$ .

Recent simulations of the Kuramoto-Sivashinsky equation [23] have shown an analogous two-cell rotating state (Fig. 13). The reflectional asymmetry of the cells is very distinctive.

### C. Counterrotating rings: Experiment

At a pressure of 1/2 atm most of the observed states have two concentric rings of cells. They appear as either stationary states or nonstationary states with various number of cells. In this section a nonstationary state with two concentric rings of six and two cells [Fig. 14(a)] is analyzed. The outer ring rotates counterclockwise at a speed of about  $360^\circ/\text{sec}$ , while the inner ring rotates clockwise at almost twice the speed.

The analysis of this state raises some important issues: determining whether the spatial structures of the rings are independent of each other, investigating the interaction of the rings and whether one can separate their dynamics, and classifying the motion of each ring as uniform or nonuniform rotation. Such analyses are difficult from direct visual observations, in part, due to the rapid motion of both rings.

The KL analysis indicates [Fig. 14(b)] the appearance of an apparently  $O(2)$ -symmetric time average. Again, one should consider that in the plane  $O(2)$  symmetry cannot be distinguished from  $SO(2)$  symmetry. The time average is similar to those of previous cases, except that now it is formed by two concentric rings. Figure 14(b) also shows

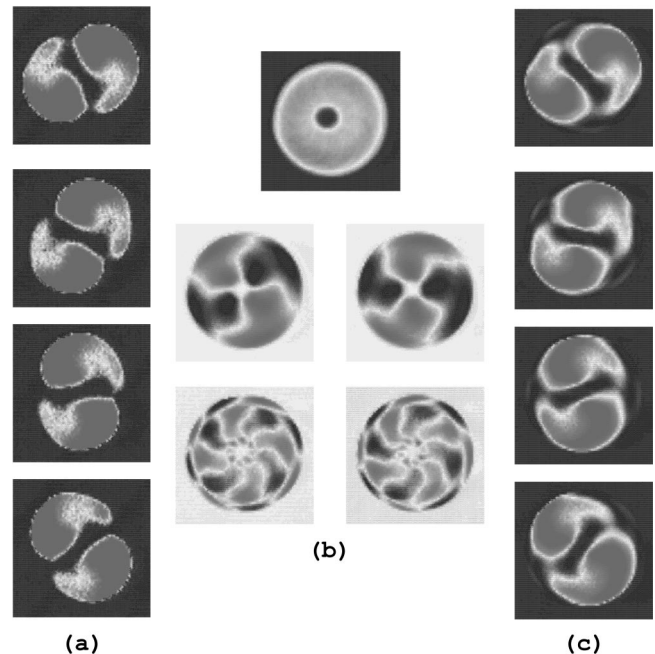


FIG. 11. (a) A two-cell rotating state found in the combustion experiment (the distinctive reflectional asymmetry of the cells is very similar to the one observed in Fig. 13), (b) the time average of the data set and (from left to right and top to bottom) the four most energetic KL modes, and (c) reconstruction of the dynamics with the four most energetic KL modes.

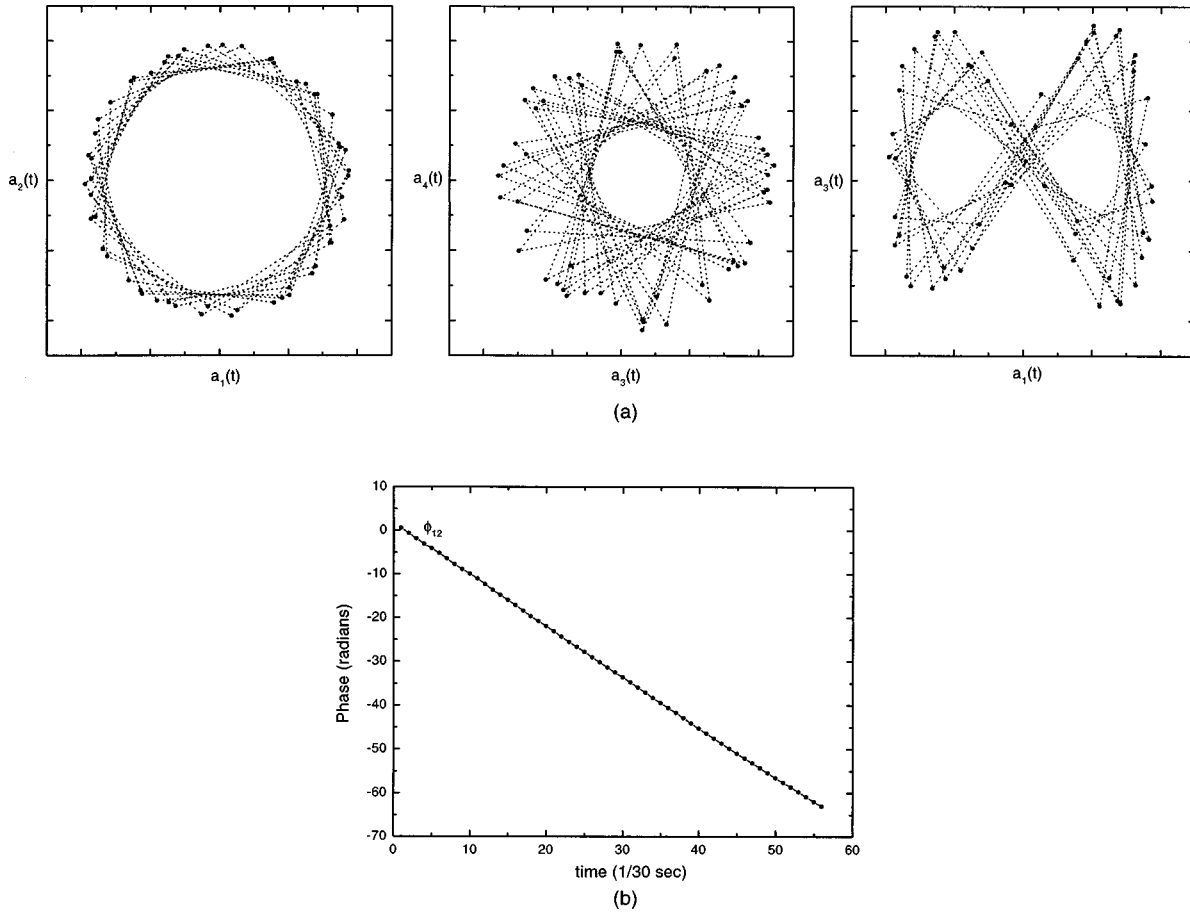


FIG. 12. Evolution of the temporal coefficients of the rotating two-cell state of Fig. 11(a): (a) from left to right phase plane plots of  $a_1(t)$  vs  $a_2(t)$ ,  $a_3(t)$  vs  $a_4(t)$ , and  $a_1(t)$  vs  $a_3(t)$  and (b) a time plot of  $\phi_{12}(t)$ .

(from left to right and top to bottom) the 12 most energetic KL modes. The separation in the spatial structures between the outer and the inner ring is clearly demonstrated. Modes  $\Phi_1$ ,  $\Phi_2$ ,  $\Phi_5$ ,  $\Phi_6$ ,  $\Phi_{11}$ , and  $\Phi_{12}$  define the structure of the outer ring, while modes  $\Phi_3$ ,  $\Phi_4$ ,  $\Phi_7$ ,  $\Phi_8$ ,  $\Phi_9$ , and  $\Phi_{10}$  represent the inner ring. In consecutive pairs (counting in increasing order from one), the modes are (approximately)  $D_6$ ,  $D_2$ ,  $D_{12}$ ,  $D_4$ ,  $D_8$ , and  $D_{18}$  symmetric, respectively. The results indicate the presence of two attractors capturing the long-term evolution (rotations) of each ring in the original state. Figure 14(c) shows the reconstructed dynamics with the eight most energetic modes. The remaining modes contain high-dimensional information that contributes to defining the shapes of the cells.

The energy spectrum (Fig. 15) further illustrates the energy distribution among different modes: 78% contained in the first four modes, 88% in the first eight, and 90% in the first twelve. Figure 15 also shows that the modes of the outer ring  $\Phi_1$ ,  $\Phi_2$ ,  $\Phi_5$ , and  $\Phi_6$  capture about 68% of the energy, compared to only 20% by the modes of the inner ring  $\Phi_3$ ,  $\Phi_4$ ,  $\Phi_7$ , and  $\Phi_8$ . This difference can be attributed to the position of the rings relative to the center of the burner and to the number of flame cells contained in each ring.

Observe that the energy is again almost equally distributed within each consecutive pair of modes. They each form an irreducible space under the action of  $\Gamma$ . The reconstructed dynamics (on each of these subspaces) corresponds to a unique branch of many symmetrically related periodic solu-

tions that appear as a consequence of the nonuniqueness of the subspaces [Proposition 3(i)]. The first eight modes are clearly the most important for the approximation. A reconstruction using only  $\Phi_1$  and  $\Phi_2$  reproduces the rotations of the outer ring with the inner ring remaining fixed. Both rings rotate when  $\Phi_3$  and  $\Phi_4$  are added to the expansion. The approximation with the next four most dominant modes improves the separation of the cells in both rings.

More details of the motion of each ring can be obtained from the phase space plots  $a_1(t)$  vs  $a_2(t)$ ,  $a_3(t)$  vs  $a_4(t)$ , and  $a_1(t)$  vs  $a_3(t)$  shown in Fig. 16(a). Connecting lines have been omitted because they obscure the structure of the points. The periodic nature of each pair of KL modes is indicated by the first two plots. The plot of  $a_1(t)$  vs  $a_3(t)$  clearly shows that the periods of the outer and inner ring are incommensurate and indicates that the underlying attractor of the system is a two-dimensional torus. The relative phases of the first two pairs of KL modes are shown in Fig. 16. The direction of rotation of each ring can be inferred from the sign of the slope of the relative phases. The figure also shows that the motion of the inner ring is strongly modulated compared to uniform motion in the outer ring.

#### D. Two-cell standing wave: Experiment

Two types of periodic solutions can bifurcate from an  $O(2) \times S^1$  symmetric state: rotating waves and standing waves. The examples studied above were rotating waves. An

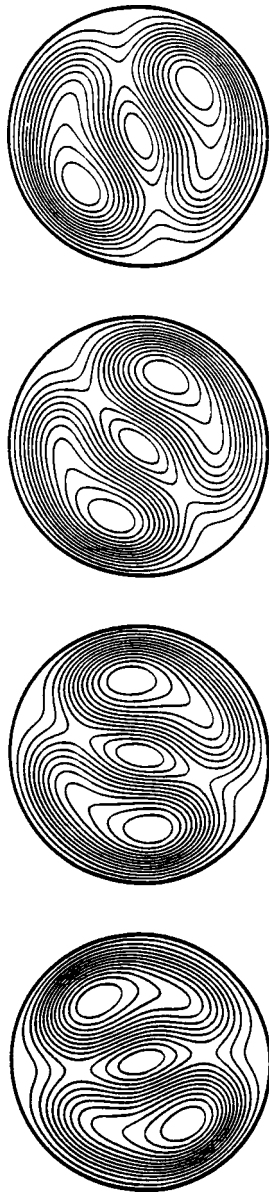


FIG. 13. Four snapshots (time varying from top to bottom) of a state with two rotating cells obtained by integrating numerically the Kuramoto-Sivashinsky equation. Note the reflectional asymmetry of the cells.

example of a standing wave is presented and analyzed next. Figure 17(a) shows a two-cell standing wave oscillating periodically between two patterns of two cells oriented at  $90^\circ$  from each other. The transitions between the two orientations occur at a rate of 1/6 sec. In Fig. 17(a), consecutive frames depicting an individual transition are shown. Figure 17(b) shows the results of the KL decomposition and Fig. 17(c) the reconstruction with the four most energetic modes. The time average is now (approximately)  $D_4$  symmetric and the first four KL modes (shown from left to right and top to bottom) are (approximately)  $D_4$ ,  $D_2$ ,  $D_4$ , and  $D_2$  symmetric, respectively. They capture about 73% of the total energy (Fig. 18).

The energy is now spread across more modes and is no longer equally distributed among consecutive pairs of modes as in previous cases. One possible explanation of the distribution is that rotating cells need two structures with equivalent energy (similar to the *sine* and *cosine* modes of the

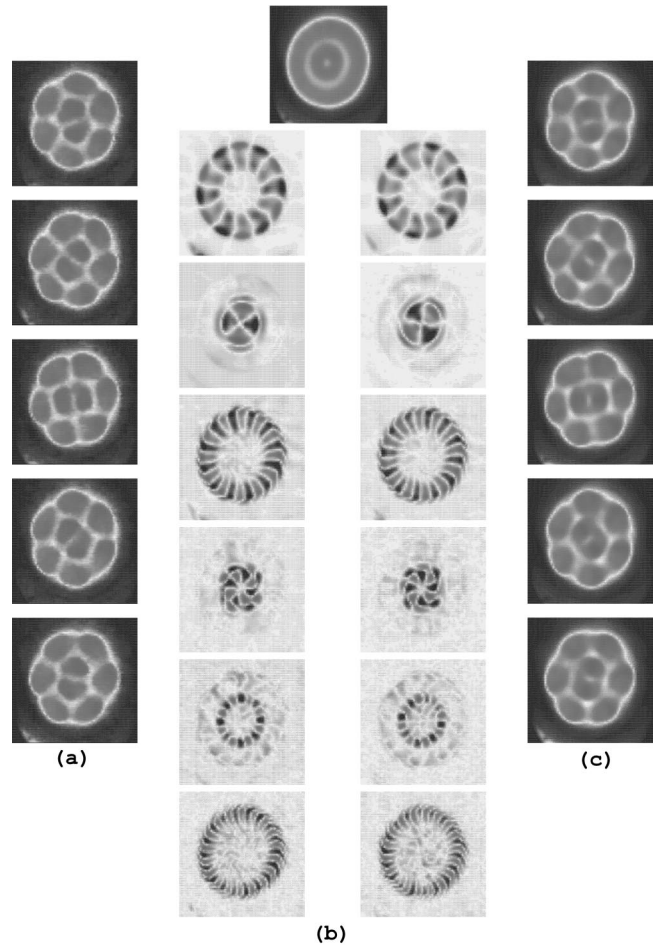


FIG. 14. (a) Four snapshots from a counterrotating ring state in the combustion experiment (the outer ring rotates counterclockwise while the inner ring rotates clockwise), (b) time-average pattern and (from left to right and top to bottom) the twelve most energetic KL modes, and (c) reconstruction of the dynamics using the eight most energetic KL modes.

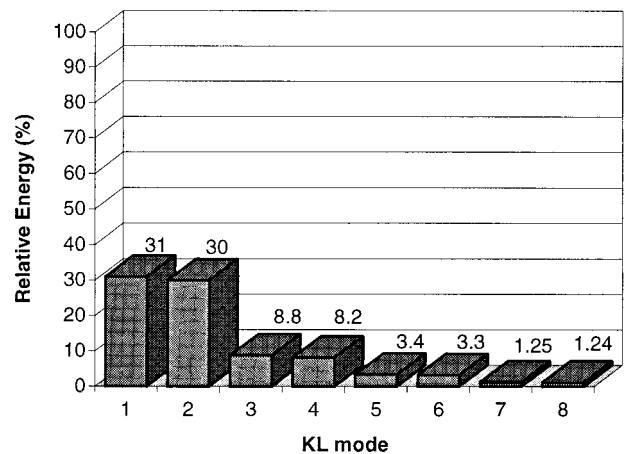


FIG. 15. Energy spectrum for the KL decomposition of the counterrotating ring state of Fig. 14(a).

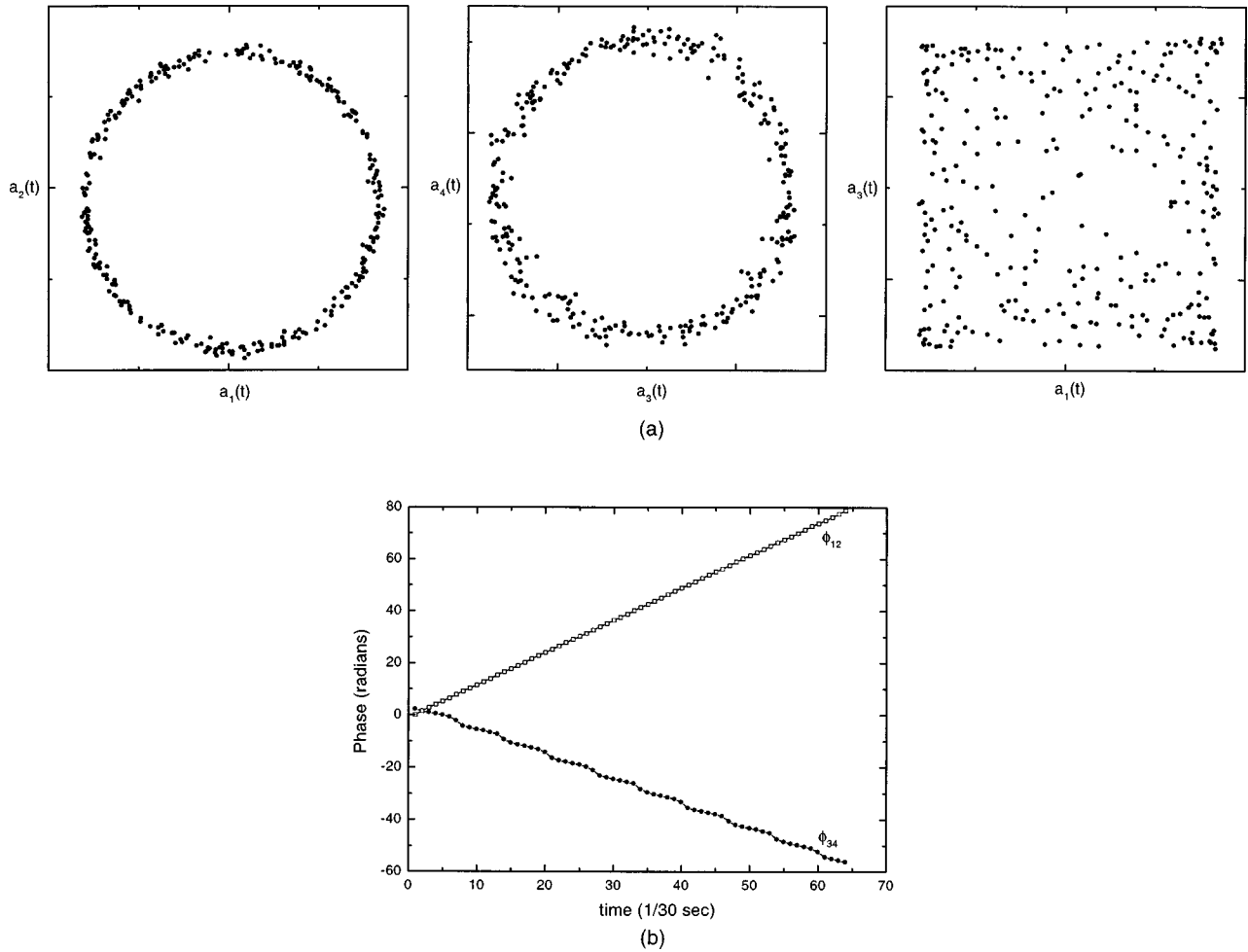


FIG. 16. Evolution of the temporal coefficients of the counterrotating ring state of Fig. 14(a): (a) from left to right phase plane plots of  $a_1(t)$  vs  $a_2(t)$ ,  $a_3(t)$  vs  $a_4(t)$ , and  $a_1(t)$  vs  $a_3(t)$  and (b) a time plot of  $\phi_{12}(t)$  and  $\phi_{34}(t)$ .

examples of Sec. III) to define the position and velocity of the cells. In contrast, the standing wave of Fig. 17(a) only needs one mode (the most energetic) to define the position and orientation of the two ordered states. The second mode is then responsible for executing the transitions between the two ordered states. These statements can be verified using Fig. 19(a), in which we have plotted the time evolution of the first two KL modes  $a_1(t)$  and  $a_2(t)$ , respectively. Observe that  $a_1(t)$  is always positive and its variations represent the fluctuations of the reconstructed pattern about the mean. The second coefficient  $a_2(t)$  oscillates between positive and negative values as the two cells in the standing wave change between the two observed orientations. Figure 19(b) further shows the phase differences between the first two KL modes. The remaining modes contain information that is used to improve the shape of the cells. The distinctive (approximately)  $D_4$  symmetry of the time average indicates that the attractor is (approximately)  $D_4$  symmetric in phase space [14].

### E. Entropy classification

The level of complexity among the flame patterns studied in this paper was calculated by applying Eq. (3.10) to the energy spectrum generated by the KL decomposition of each

individual state. The results are presented in the following table.

Description of state	Entropy
experimental one-cell state rotating	0.540010
modeled one-cell state rotating uniformly	0.250941
modeled one-cell state rotating nonuniformly	0.311503
experimental two-cell state rotating	0.421630
experimental counterrotating rings	0.513859
experimental standing wave	0.587134

The results indicate that the uniform and nonuniform rotating states of the phenomenological model have the lowest entropy followed by the uniform rotating two-cell state in the experiment. High-entropy values can be attributed to shape behavior in the cells. When a state exhibits strong shape changes, as in the case of the experimental single-cell state, its energy spectrum is broad and thus produces a high entropy. In contrast, when the cells show very little change in shape, as in the counterrotating rings from the experiment, the energy is distributed among fewer modes, resulting in a lower-entropy measure. Observe that the highest entropy was exhibited by the standing wave, as one would expect from its broad energy profile.

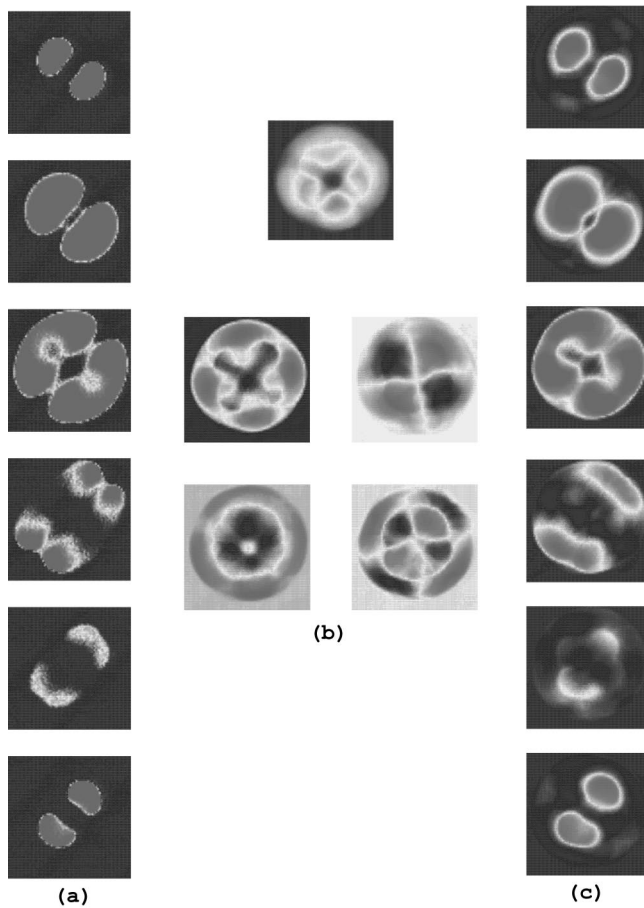


FIG. 17. (a) A standing wave between patterns of two cells oriented at  $90^\circ$  angles from each other, (b) the time-average pattern has a well-defined  $D_4$  symmetry and the first four most energetic modes (from left to right and top to bottom) capture about 73% of the total energy, and (c) the reconstruction using the four most energetic KL modes is very close to the original cycle.

## V. DISCUSSION

The review by Cross and Hohenberg [24] describes a number of systems that exhibit pattern formation. Almost all of the experimental studies of these systems used large-aspect-ratio geometries that contain large numbers of cells or

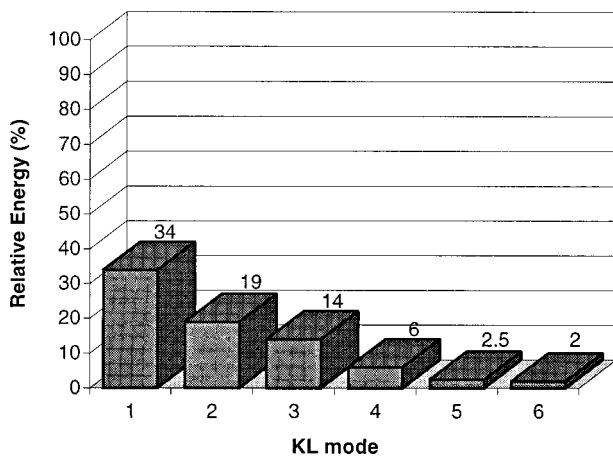


FIG. 18. Energy spectrum for the KL decomposition of the two-cell standing wave shown in Fig. 17(a).

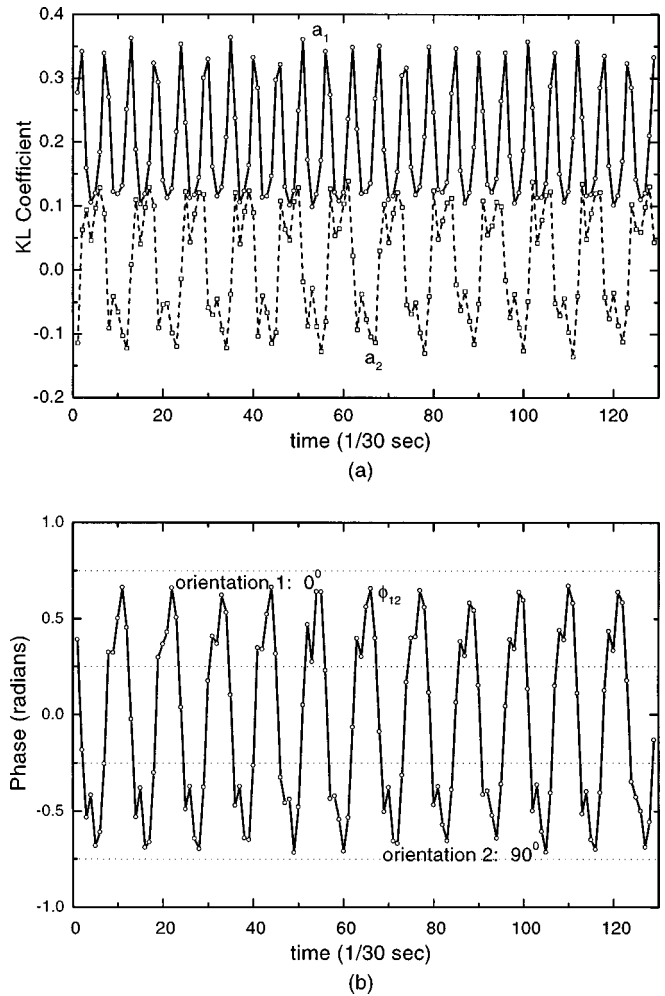


FIG. 19. Evolution of the temporal coefficients of the standing-wave state of Fig. 17(a): (a) time plots of  $a_1(t)$  and  $a_2(t)$  and (b)  $\phi_{12}(t)$  depicts the phase transitions between two ordered states oriented at  $90^\circ$  angles with respect to each other.

stripes. KL analysis has been used on other systems exhibiting two-dimensional spatiotemporal dynamics. Graham, Lane, and Luss [25] used KL analysis to study temperature patterns in a chemically reacting system. More recently Sirovich *et al.* [26] used these techniques in the analysis of video images of the mammalian visual cortex system. The results indicated a relationship between the KL eigenfunctions and the orientational and directional information of the visual system.

Premixed flames are not typical of systems exhibiting spatiotemporal dynamics. Pulsating [27] and cellular flames exhibit a substantial ( $>50$ ) number of periodic and chaotic dynamic states that execute complex spatiotemporal dynamics. The stability boundary diagrams of these states are complicated and many different types of bifurcations between states are observed.

At least five different types of dynamic states of cellular flames (rotating, modulated rotating, standing wave, hopping, and ratcheting) have relatively low-dimensional dynamics that can be captured by a few ( $<10$ ) KL modes. The precise characterization of their dynamics cannot be determined either from direct visual observation or from a frame-by-frame analysis of videotape. In these cases a KL analysis

is used to provide a description of the modes that comprise the dynamics. In this paper we have concentrated on four representative examples of three types of states with small numbers of cells: rotating states, modulated rotating states, and standing-wave states. We have demonstrated that KL analysis is particularly useful in distinguishing between uniform and nonuniform rotation. The periodic two-cell standing-wave state presents an interesting, contrasting example to the periodic two-cell rotating state. A KL analysis of counterrotating double rings demonstrates the physical separation of the dynamics into the two rings. We have also included a KL analysis of rotating and modulated rotating states from a phenomenological model to compare and contrast these results with those from similar states in the ex-

periment. Throughout the paper we have emphasized the implications of the symmetries of the KL modes.

#### ACKNOWLEDGMENTS

We would like to thank M. Golubitsky, B. Matkowsky, and I. Melbourne for many fruitful discussions and suggestions and D. Zhang, G. Wei, D. Kouri, and D. Hoffmann for providing the results of the integrations from the Kuramoto-Sivashinsky equation. This work was partially funded by the Office of Naval Research through Grant No. N-00014-K-0613 and by the Energy Laboratory at The University of Houston.

- 
- [1] E. Stone, D. Armbruster, and R. Heiland, *Fields Inst. Commun.* **5**, 1 (1996).
- [2] A. Palacios, D. Armbruster, E. Kostelich, and E. Stone, *Physica D* **96**, 132 (1996).
- [3] A. Palacios, G. H. Gunaratne, M. Gorman, and K. A. Robbins, *Chaos* **7**, 463 (1997).
- [4] M. Golubitsky, I. Stewart, and D. G. Schaeffer, *Singularities and Groups in Bifurcation Theory* (Springer-Verlag, New York, 1988), Vol. 2.
- [5] M. Gorman, C. Hamill, M. El-Hamdi, and K. Robbins, *Combust. Sci. Technol.* **98**, 25 (1994).
- [6] P. Holmes, J. Lumley, and G. Berkooz, *Turbulence, Coherent Structures, Dynamical Systems and Symmetry* (Cambridge University Press, Cambridge, 1996).
- [7] K. Karhunen, *Ann. Acad. Sci. Fennicae Ser. A* **1**, 34 (1944).
- [8] M. Loève, *Probability Theory* (Van Nostrand, New York, 1955).
- [9] J. L. Lumley, in *Atmospheric Turbulence and Radio Wave Propagation*, edited by A. M. Yaglom and V. I. Tatarski (Nauka, Moscow, 1967), p. 166.
- [10] L. Sirovich, *Q. Appl. Math.* **5**, 561 (1987).
- [11] F. Riesz and B. Sz.-Nagy, *Functional Analysis* (Dover, New York, 1990).
- [12] J. K. Hale, *Ordinary Differential Equations* (Wiley, New York, 1980).
- [13] N. Aubry, R. Guyonnet, and R. Lima, *J. Nonlinear Sci.* **2**, 183 (1992).
- [14] M. Dellnitz, M. Golubitsky, and M. Nicol, in *Trends and Perspectives in Applied Mathematics*, edited by L. Sirovich (Springer-Verlag, New York, 1994), Vol. 100, p. 73.
- [15] D. Armbruster, R. Heiland, and E. Kostelich, *Chaos* **4**, 421 (1993).
- [16] Computer animations illustrating side by side comparisons between different KL reconstructions of flame patterns can be found at the web address <http://vip.cs.utsa.edu/flames/klvisual/klvisual.html>.
- [17] P. Coullet, R. Goldstein, and G. H. Gunaratne, *Phys. Rev. Lett.* **63**, 1954 (1989).
- [18] R. Goldstein, G. H. Gunaratne, L. Gil, and P. Coullet, *Phys. Rev. A* **43**, 6700 (1991).
- [19] G. Gunaratne, M. El-Hamdi, M. Gorman, and K. Robbins, *Mod. Phys. Lett. B* **10**, 1379 (1996).
- [20] L. Sirovich (private communication).
- [21] Y. Kuramoto, *Prog. Theor. Phys. Suppl.* **64**, 346 (1978).
- [22] G. I. Sivashinsky, *Acta Astron.* **4**, 1176 (1977).
- [23] D. S. Zhang, G. W. Wei, D. J. Kouri, D. K. Hoffmann, M. Gorman, G. Gunaratne, and A. Palacios (unpublished).
- [24] M. Cross and P. Hohenberg, *Rev. Mod. Phys.* **65**, 851 (1993).
- [25] M. Graham, S. Lane, and D. Luss, *J. Phys. Chem.* **97**, 889 (1993).
- [26] L. Sirovich, R. Everson, E. Kaplan, B. Knight, E. O'Brien, and D. Orbach, *Physica D* **96**, 355 (1996).
- [27] M. Gorman, C. Hamill, M. El-Hamdi, and K. Robbins, *Combust. Sci. Technol.* **98**, 47 (1994).